ACS OMEGA

Open Access

http://pubs.acs.org/journal/acsodf

Article

Silicon Monoxide Anodes Co-Modified with ZnS and Nitrogen-Doped Carbon via Facile Synthesis: Toward High-Energy Lithium-Ion Battery Applications

Yongchao Liu, Hongliang Mu, Liu Feng,* Wuhong Xin, Jinye Niu, Xuliang Zhang,* Yong Wang, and Guanghui Li

Cite This: *ACS Omega* 2025, 10, 17642−17650

Read Online

ACCESS | Metrics & More | Article Recommendations

ABSTRACT: Silicon monoxide (SiO) has emerged as a promising silicon-based anode material owing to its high theoretical specific capacity and extended cycle life. Nevertheless, its practical application is hindered by significant volume expansion and insufficient cycling stability. In this study, a composite material of SiO coated with zinc sulfide and nitrogen-doped carbon (ZnS&NC/SiO) was successfully prepared via a developed method of in situ conversing MOFs into nitrogen-doped carbon and ZnS. As an anode of lithium-ion batteries, the ZnS&NC/SiO composite exhibited superior reversible capacity (748 mAh·g^{-1} after 1000 cycles at 1.0 A·g^{-1}) and ultralower electrochemical impedance spectra (Rct = 62 Ω). The performance is much superior to that of the reported SiO-based anode materials, which is attributed to the special coating structure that relieves volume expansion and improves the inherently low electrical conductivity, the doped N atoms that provide more active sites, and the SiO and ZnS enables one of them to serve as a buffer medium for more stable structure due to the different lithium intercalation potential. The designed structure could provide a promising strategy for other electrode materials.

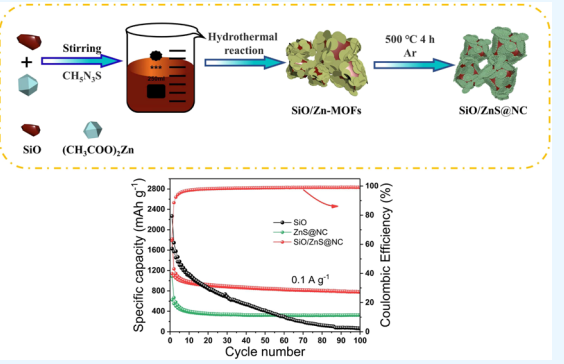

1. INTRODUCTION

Conventional lithium-ion batteries utilizing graphite anodes currently face inherent limitations in meeting the energy density requirements of electric vehicles (EVs) and associated applications, primarily stemming from their constrained electrochemical capacity.[1−7] Consequently, the development of advanced anode materials with enhanced specific capacity and cycling stability is critically imperative to address the current limitations in lithium-ion battery technologies. The advanced properties of silicon monoxide (SiO), such as high theoretical capacity (2600 mAh·g^{-1}), abundant reserves, and environmental friendliness, make it an ideal material for the next generation of lithium-ion batteries. However, the commercialization of silicon monoxide faces challenges due to its significant volume expansion and insufficient electrical conductivity during lithiation and delithiation processes.[8−11]

To address the aforementioned issues, various effective strategies have been investigated, which mainly focus on SiO self-modifying and compositing with other materials. Among these methods, the construction of biphasic structures is a proven effective strategy. Carbon is extensively utilized due to its superior electrical conductivity; for instance, Wang et al.[12] synthesized a SiO/C composite featuring a network-like carbon coating layer through a two-step process involving spray-drying followed by pyrolysis. The resulting composite exhibits a sustained capacity of 577.7 mAh·g^{-1} even after 100 cycles at a current density of 1 A·g^{-1}. Zhang et al.[13] fabricated SiO nanoparticles embedded in hierarchical porous N-doped carbon nanosheets through ball-milling and annealing treatment. These N-doped carbon nanosheets not only minimize volume variations but also enhance the reaction kinetics.

Another novel electrode structure consisting of two lithium-embedding materials was designed, such as SnO_2/Co_3O_4, SnO_2/Fe_3O_4, ZnO/TiO_2, and TiO_2/SnO_2,[14−17] which all exhibit different reactivity potentials during the lithiation process. When the active material reacts with lithium, the inactive material provides a good buffering effect on volume variations, thereby enhancing the stability of the electrode material. Among these materials, ZnS has attracted considerable attention because of its abundant sources, low cost, and

Received: December 24, 2024
Revised: February 27, 2025
Accepted: April 10, 2025
Published: April 25, 2025

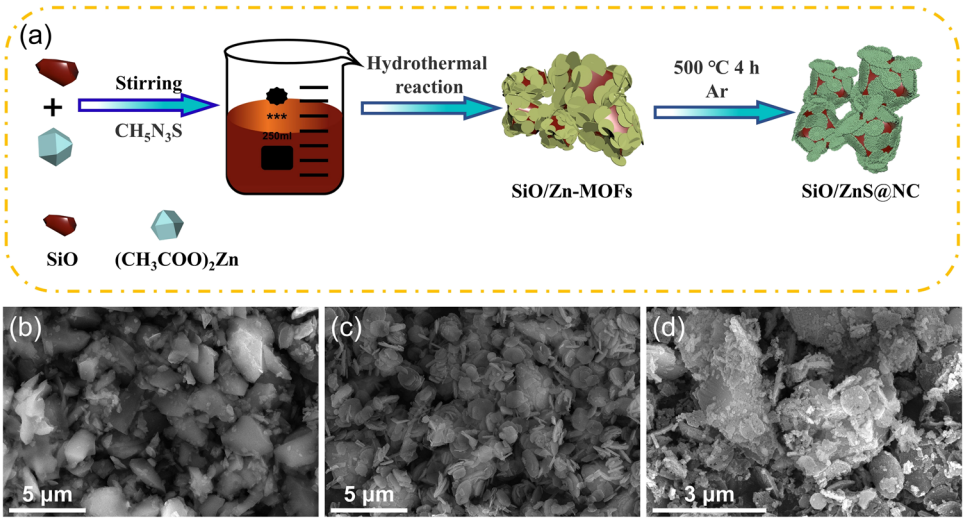

Figure 1. (a) Schematic illustration of the preparation process of ZnS&NC/SiO composites. SEM images of (b) SiO, (c) SiO/Zn-MOF, and (d) ZnS&NC/SiO.

high theoretical capacity (962 mAh·g^{-1}). For example, Gu et al.[18] fabricated hollow structured SnO_2/ZnS@C composite via a hydrothermal reaction and a carbon coating process. The resulting sample exhibits a capacity of 753.5 mAh·g^{-1} at 0.1 A·g^{-1} over 200 cycles.

Based on the above investigations, it is proposed that simultaneously introducing ZnS and N-doped carbon materials represents a promising strategy for alleviating the volume expansion and enhancing the electrical conductivity of SiO during lithiation and delithiation processes, and the related studies have rarely been reported to the best of our knowledge. In this paper, SiO material coated with ZnS and N-doped carbon was fabricated (ZnS&NC/SiO) through a simple hydrothermal reaction followed by heat treatment. It is shown that the ZnS&NC/SiO composite exhibited superior electrochemical performance when employed as anodes in Li-ion batteries, with a reversible capacity of 748 mAh·g^{-1} maintained after 1000 cycles at a current density of 1.0 A·g^{-1}. It is suggested that the enhanced performance is attributed to a synergistic effect between introduced ZnS and nitrogen-doped carbon. The outer carbon layer can effectively improve the inherently low electrical conductivity of SiO, concurrently preventing the chalking and shedding of the electrodes. The doped N atoms can afford more active sites for Li^+ storage. The different lithium intercalation potentials between SiO and ZnS allow one of them to serve as a buffer medium to alleviate volume expansion when the other material undergoes lithium intercalation, leading to improved structural stability of the electrode. This work provides a feasible strategy for fabricating anode materials with exceptional electrochemical properties, high specific capacity, and excellent cycling performance for Li-ion batteries.

2. EXPERIMENTAL METHODS

All chemicals were of analytical grade and used as received without further purification. Deionized water was used throughout the experiments.

2.1. Materials Preparation. ZnS&NC/SiO composite was synthesized via a simple hydrothermal reaction and subsequent heat treatment, and the method details are described below:

(1) Preparation of SiO/Zn-MOF, Zn-MOF: 1 mmol of SiO power (1−3 μm) was evenly dispersed in 20 mL of methyl alcohol and 20 mL of N,N-dimethylformamide (DMF) using a magnetic stirrer for 30 min, and then 1 mmol of zinc acetate $(CH_3COO)_2Zn$ was added to the above suspension holding for 30 min, denoted as solution A. Concurrently, 3 mmol of thiosemicarbazide (TSC) was added to 20 mL of methyl alcohol and 20 mL of DMF to form another solution B. Solution B was then poured into solution A with continuous stirring, and stirred for 40 min. Consequently, the mixed solution was transferred into a 100 mL Teflon-lined stainless autoclave and placed in an oven at 120 °C for 6 h. Finally, the as-prepared reactant, labeled as SiO/Zn-MOF, was collected by centrifugation, washed with water and ethanol at least five times, and dried in a vacuum oven at 80 °C for 12 h. For comparison, Zn-MOF was prepared under the same conditions without SiO.

(2) Preparation of ZnS&NC/SiO, ZnS&NC: SiO/Zn-MOF was annealed under an Ar atmosphere at 500 °C for 4 h with a heating rate of 3 °C/min to obtain the ZnS&NC/SiO composite. Similarly, ZnS@NC samples were prepared from Zn-MOF under the same experimental conditions.

2.2. Material Characterization. The surface morphology and microstructure of the samples were characterized by scanning electron microscopy (SEM, Apero S), transmission electron microscopy (TEM, Tecnai G^2 F20, 200 kV), and high-resolution TEM (HRTEM) equipped with an energy-dispersive X-ray (EDX) spectrometer. The specific surface area was calculated by using Brunauer−Emmett−Teller (BET), and pore diameter distribution plots were obtained by the N_2 adsorption/desorption isotherms on a JWGB, JW-BK200C tester. Thermal gravimetric analysis (TGA) was carried out in an Ar environment with a thermal analyzer (SDT-Q650), and the heating rate was 10 C min^{-1}. The crystalline structure feature of the samples was characterized by X-ray diffraction (XRD, D/MAX-IIIC) with Cu Kα radiation at a scan rate of 4° min^{-1} in the range of 10−90°. The element valence and bonding configuration on the sample's surface was analyzed

https://doi.org/10.1021/acsomega.4c11551
ACS Omega 2025, 10, 17642−17650

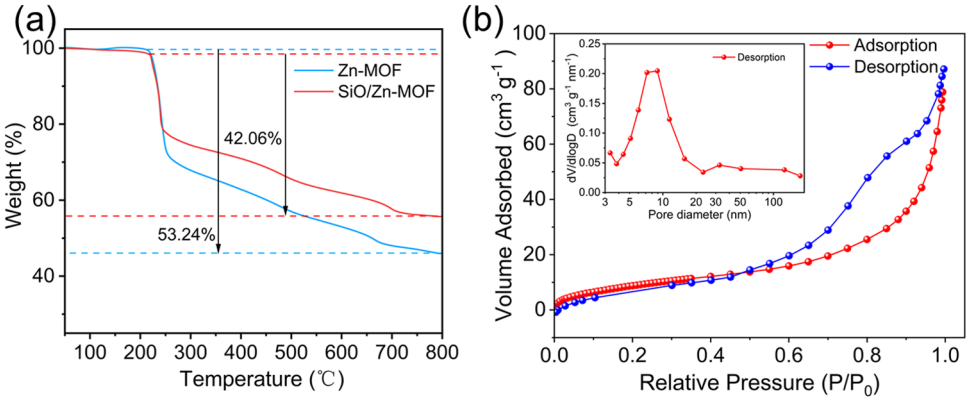

Figure 2. (a) TGA curves of Zn-MOF and SiO/Zn-MOF. (b) Nitrogen adsorption−desorption isotherm curves of ZnS&NC/SiO (the illustration shows the pore size distribution curve).

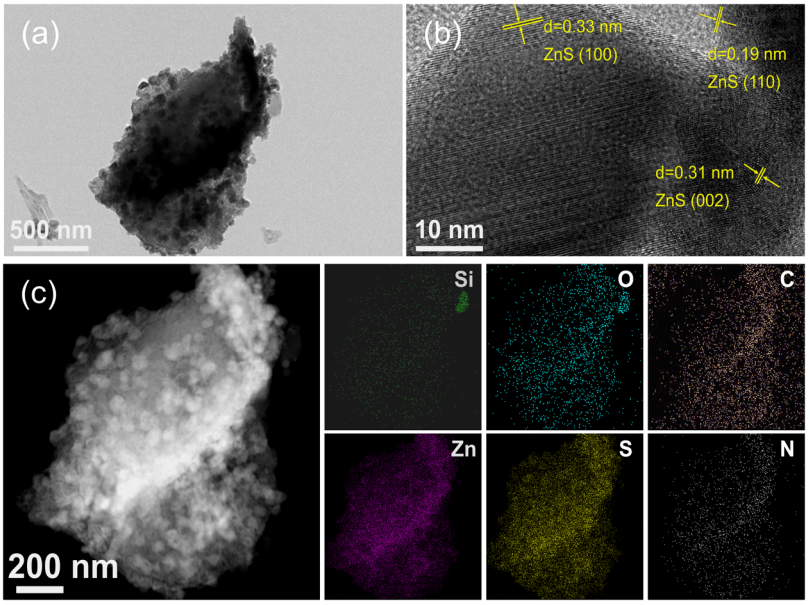

Figure 3. (a) TEM, (b) HRTEM, (c) HADDF-STEM, and elemental mapping images of the ZnS&NC/SiO (Si, O, C, Zn, S, N).

with X-ray photoelectron spectroscopy (XPS, ESCALAB 250Xi).

2.3. Electrochemical Measurements. The working electrode paste was prepared by homogeneously integrating active materials, acetylene black, and carboxymethyl cellulose (CMC) in a mass ratio of 6:2:2 into deionized water. The copper foil was subsequently coated in a uniform layer with the resultant paste and subjected to drying in a vacuum oven at 80 °C for a duration of 12 h.

Coin-type half cells (CR 2032) were meticulously assembled within a glovebox under an argon atmosphere, utilizing the aforementioned electrode as the working electrode, lithium foil as the reference electrode, and Celgard 2500 as the separator. The electrolyte comprised 1 M $LiPF_6$ in a solvent mixture of EC/DMC/EMC in a volume ratio of 1:1:1, enriched with 10% fluoroethylene carbonate (FEC) and 2% vinylene carbonate (VC). Cell capacity, cycling stability, and rate capability were evaluated using galvanostatic charge−discharge cycling within a voltage range of 0.01 to 2.5 V (versus Li/Li^+) on a Neware-CT4008T battery testing system. The cyclic voltammetry (CV) analysis was performed with a scan rate of 0.1 mV s^{-1} and a voltage window range of 0.01−2.5 V, respectively, and the electrochemical impedance spectroscopy (EIS) tests were conducted at frequencies ranging from 0.01 to 10^5 Hz; both were tested on a CHI 660B electrochemical workstation.

3. RESULTS AND DISCUSSION

The MOF-derived ZnS&NC/SiO was successfully synthesized with the schematic illustrated in Figure 1a. Initially, flake Zn-MOF was grown on the SiO surface during the hydrothermal process. Subsequently, the resulting SiO/Zn-MOF material transformed into the ZnS&NC/SiO composite through heat treatment. Surface morphological characteristics of the samples were analyzed by utilizing scanning electron microscopy (SEM), as shown in Figure 1b−d. The employed pristine SiO powder was granular in form with an average particle size of 1 μm, as shown in Figure 1b. The granular morphology of SiO is also discernible on the SiO/Zn-MOF sample, which is coated with Zn-MOF flakes, as illustrated in Figure 1c. Following high-temperature calcination, it was clearly observable that the extensive SiO surface was enveloped by ZnS particles, with distinct flake-like ZnS dispersed upon or around the SiO particles, as shown in Figure 1d.

https://doi.org/10.1021/acsomega.4c11551
ACS Omega 2025, 10, 17642−17650

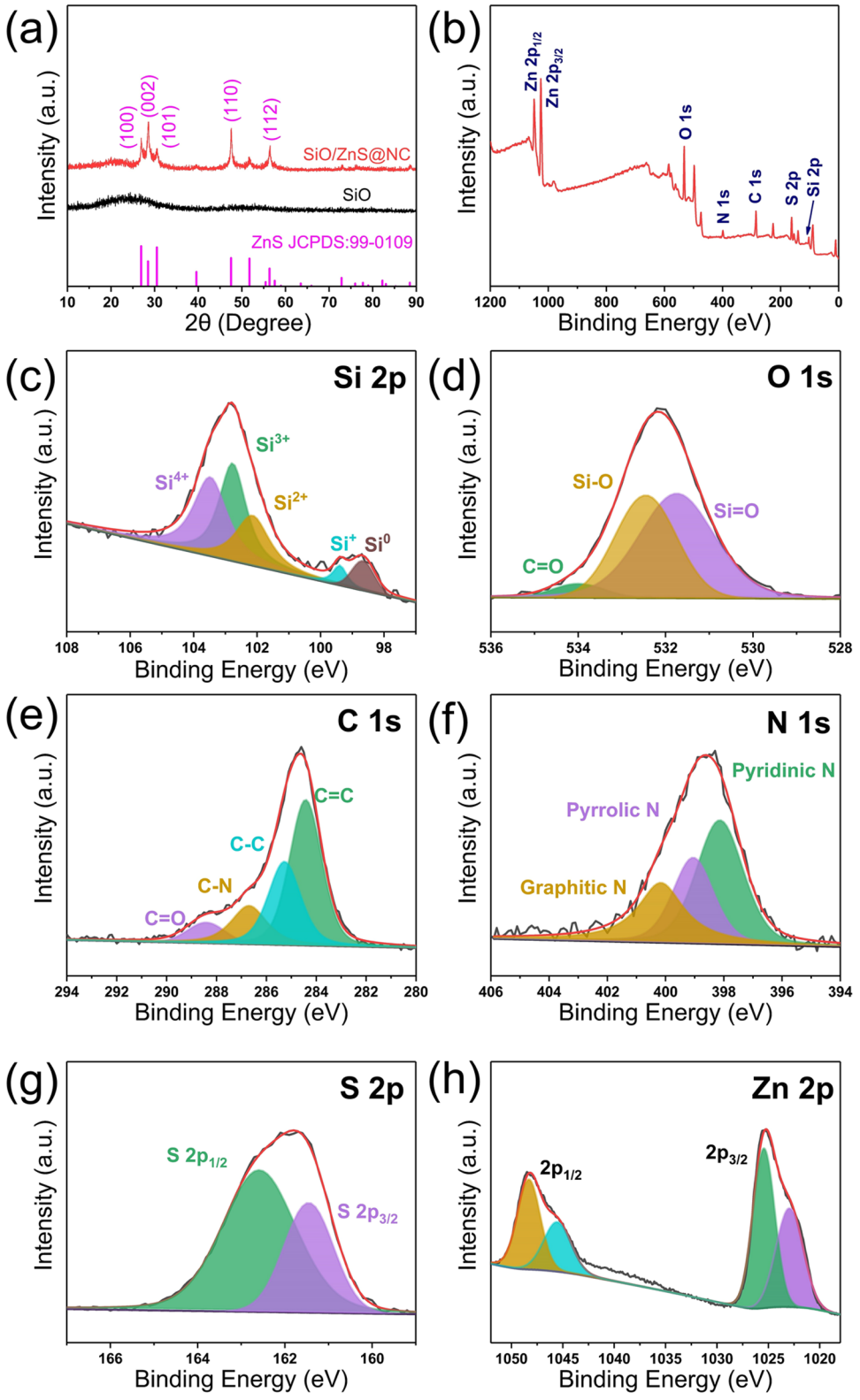

Figure 4. (a) XRD pattern of SiO and ZnS&NC/SiO, (b) the survey XPS spectra of the ZnS&NC/SiO, high-resolution XPS spectra of ZnS&NC/SiO: (c) Si 2p, (d) O 1s, (e) C 1s, (f) N 1s, (g) S 2p, and (h) Zn 2p.

To explore the calcination temperature, TGA was employed to investigate the thermal decomposition behavior of the Zn-MOF and SiO/Zn-MoF composites, as shown in Figure 2a. The curve exhibits a slight downward trend between room temperature and 150 °C, which is attributed to the evaporation of surface-bound water from the sample. Subsequently, the curve demonstrates a sharp decline starting at 200 °C, a phenomenon resulting from the pyrolysis of Zn-MOF, corresponding to the formation of ZnS and nitrogen-doped carbon materials. Beyond 700 °C, the curve tends to stabilize,

https://doi.org/10.1021/acsomega.4c11551
ACS Omega 2025, 10, 17642−17650

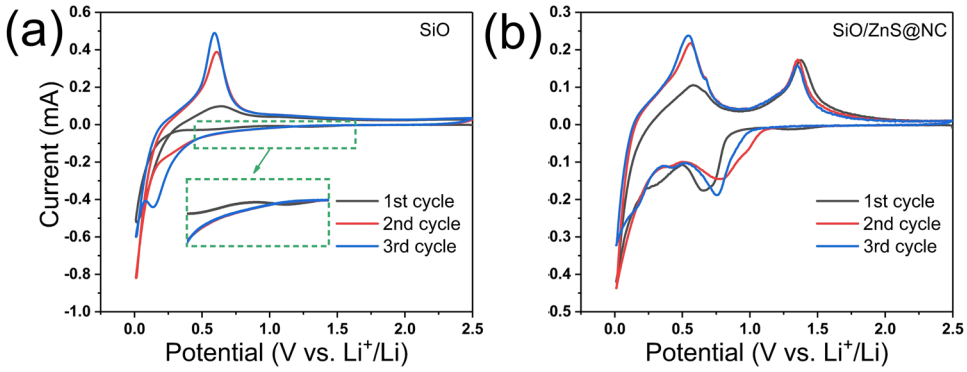

Figure 5. CV curves of the (a) SiO and (b) ZnS&NC/SiO at a scan rate of 0.1 mV s^{-1}.

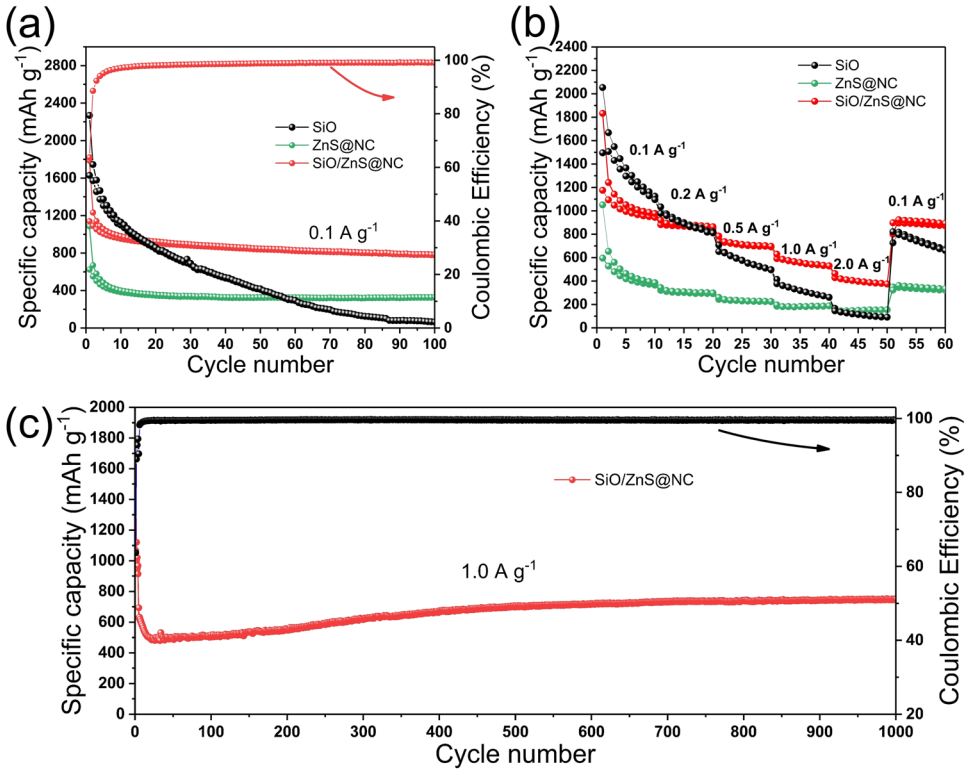

Figure 6. Lithium storage properties. (a) Cyclic performance of the SiO, ZnS&NC, and ZnS&NC/SiO at 0.1 A·g^{-1}; (b) rate capabilities of the SiO, ZnS&NC, and ZnS&NC/SiO; and (c) cyclic performance of the ZnS&NC/SiO at 1.0 A·g^{-1}.

indicating near-completion of the thermal decomposition process. The SiO/Zn-MOF composites and Zn-MOF exhibit distinct mass losses of 40.04 and 53.26%, respectively.

In order to measure the specific surface area of the ZnS&NC/SiO composites, a nitrogen adsorption−desorption experiment was performed, as shown in Figure 2b. The BET-specific surface area of the ZnS&NC/SiO was 36 m^2 g^{-1}, which was attributed to the nitrogen-doped carbon materials. The illustration illustrates the pore size distribution of the sample, indicating that the composites predominantly exhibit pores around 9 nm, thereby confirming its mesoporous nature.

The microstructure of the ZnS&NC/SiO composite was further verified through high-resolution transmission electron microscopy (HRTEM) and energy-dispersive X-ray spectroscopy (EDS), with the corresponding images displayed in Figure 3. Figure 3a reveals that the surface of SiO particles is covered with a layer of C and ZnS, including particles and intact flake-like structures distributed evenly. The high-resolution TEM (HRTEM) image in Figure 3b indicates that the d-spacings of approximately 0.33, 0.19, and 0.31 nm correspond to (100), (110), and (002) crystal planes of the ZnS phase, respectively. Figure 3c showcases the HAADF-STEM and EDS elemental mapping images of the ZnS&NC/SiO composite, illustrating a homogeneous distribution of Si, O, C, Zn, S, and N elements, which corroborates the dispersion of nitrogen-doped carbon and ZnS on the SiO surface.

The phase compositions and crystallinity of the SiO and ZnS&NC/SiO samples were measured by XRD analysis, as shown in Figure 4a. The XRD patterns of the pristine SiO samples exhibited a wide diffraction peak located around 23°, suggesting an amorphous phase composition in alignment with the previous reports.[19−21] The ZnS&NC/SiO composite exhibits four sharp diffraction peaks at 2θ = 26.9, 28.5, 30.5, 47.5, and 56.3°, which are related to the formation of ZnS,

https://doi.org/10.1021/acsomega.4c11551
ACS Omega 2025, 10, 17642−17650

Table 1. Comparison of the Cyclic Properties between ZnS&NC/SiO and Reported SiO_x/Metal Compound Electrodes

sample	current density ($A{\cdot}g^{-1}$)	cycle number	capacity ($mAh{\cdot}g^{-1}$)	ref
ZnS&NC/SiO	0.1	100	776	this work
	1.0	1000	748	this work
p-SiO/TiO_2 (B)-1	0.1	100	730	40
SiO@C/$BaTiO_3$/CNTs	0.1	200	712	41
(SiO+G) /CNTs	0.1	125	466	42
MnO-SiO_x@C	0.3	100	732	43
SiO_x/C/CoO	0.5	600	485	44
3% TC-SiO	0.7	450	400	45
SiO/ZrO_2	0.8	100	721	46
Sn_2Fe@30SiO_x	1.0	1200	600	47

corresponding to the crystal planes of ZnS (JCPDS:99-0109).[22,23]

The chemical composition and surface electronic states of the ZnS&NC/SiO samples were characterized using X-ray photoelectron spectroscopy (XPS). As shown in Figure 4b, the survey XPS spectra showed that there were Si, O, C, Zn, S, and N elements in the ZnS&NC/SiO samples, which was consistent with EDS (Figure 3c). The survey XPS spectrum, shown in Figure 4b, indicates the presence of Si, O, C, Zn, S, and N elements in the ZnS&NC/SiO sample, supporting the EDS results mentioned above. The high-resolution Si 2p spectrum, as shown in Figure 4c, exhibits five peaks at 98.66, 99.39, 102.14, 102.77, and 103.48 eV, corresponding to the Si^0, Si^+, Si^{2+}, Si^{3+}, and Si^{4+}, which is consistent with XRD results on the amorphous phase composition of SiO, respectively.[24,25] Figure 4d for the high-resolution spectrum of O 1s exhibits three typical peaks at 531.74, 534.00, and 532.45 eV corresponding to Si = O, Si−O, and C = O bonds, respectively.[26] The C 1s peak (Figure 4e) is deconvoluted into four subpeaks at 284.42, 285.27, 286.69, and 288.41 eV, which can be assigned to C = C, C−C, C−N, and C = O bonds.[27] The N 1s spectrum, as shown in Figure 4f, is deconvoluted into three peaks centered at 398.13, 399.05, and 400.16 eV, corresponding to pyridinic N, pyrrolic N, and graphitic N, respectively.[28] Based on the C 1s and N 1s results, it is indicated that the N-doped carbon material is successfully introduced. The S 2p spectrum in Figure 4g exhibits two peaks at 161.45 and 162.59 eV, which can be assigned to S $2p_{3/2}$ and S $2p_{1/2}$, respectively.[29] The Figure 4h for the high-resolution XPS spectrum of Zn 2p is split into two peaks at 1025.30 and 1048.12 eV, which can be assigned to Zn $2p_{3/2}$ and Zn $2p_{1/2}$ of Zn^{2+}, respectively.[30,31]

Figure 5 shows the cyclic voltammetric (CV) profiles of SiO and ZnS&NC/SiO within the potential range of 0.01 to 2.5 V, acquired at a scan rate of 0.1 $mV{\cdot}S^{-1}$. The broad cathodic peaks at 1.26 and 0.64 V observed in the initial reduction process for SiO did not reappear in the subsequent cycles, and this phenomenon can be attributed to the formation of the solid electrolyte interphase (SEI) layer and the initial insertion of Li ions into SiO.[32,33] For SiO (Figure 5a), the cathodic peak observed in the range of 0.01−0.2 V corresponds to the electrochemical reaction between Li^+ and SiO, resulting in the formation of Li−Si alloys, Li_2O, and lithium silicates.[34] The presence of Li_2O and lithium silicates is beneficial for preventing the agglomeration of SiO during the cycling process and alleviating the degree of volume expansion during lithium intercalation. During the subsequent oxidation phase, the strong anodic peak at 0.59 V can be attributed to the lithium's removal from the Li−Si alloy.[35] Figure 5b presents the first three cyclic voltammetric (CV) curves for the ZnS&NC/SiO composite. The cathodic peak at 1.34 V can only be observed in the initial cycle, which corresponds to the formation of the SEI layer during the first lithium insertion of SiO.[32,33] The peak at 0.65 V corresponds to the reaction of Li^+ with ZnS to form Li_2S and Zn, while the cathodic peak at 0.32 V is associated with the conversion reaction of Li_xZn alloy and the SEI layer.[36] The cathodic peak observed in the range of 0.01−0.2 V indicates the reaction between Li^+ and SiO, resulting in the synthesis of Li−Si alloy, Li_2O, and lithium silicates. In the first-cycle anodic scan, the oxidation peak at 0.58 V corresponds to the dealloying reaction of the Li_xSi alloy. Additionally, the dealloying reaction of the Li_xZn alloy, which leads to the formation of Zn and Li_2S, occurs between 0.2 and 0.7 V. However, only the oxidation peak at 0.67 V is observable, overshadowed by the dominant LixSi dealloying reaction. The oxidation peak at 1.40 V is attributed to the regeneration of ZnS.[37−39] During the subsequent scans, a notable shift of the oxidation peak from 0.32 and 0.65 to 0.42 and 0.76 V, respectively, was observed, potentially attributable to structural reorganization.[36]

The cyclic performance curves of SiO, ZnS&NC, and ZnS&NC/SiO at a current density of 0.1 $A{\cdot}g^{-1}$ are shown in Figure 6a, and the pristine SiO electrode shows the highest initial discharge capacity of 2269 $mAh{\cdot}g^{-1}$. However, this capacity experienced a dramatic decay over successive cycles, and the reversible capacity is only 66 $mAh{\cdot}g^{-1}$ after 100 circles. Similarly, the ZnS&NC material exhibits an initial discharge capacity of 1086 $mAh{\cdot}g^{-1}$, and the reversible capacity remains only 326 $mAh{\cdot}g^{-1}$ after 100 circles. In contrast, the ZnS&NC/SiO composite exhibits outstanding cyclic performance, and

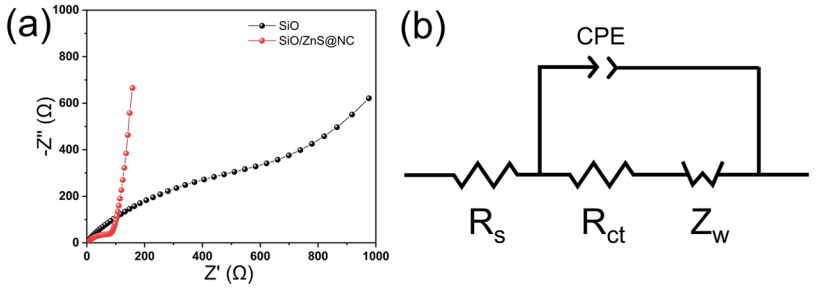

Figure 7. (a) Nyquist plots of the SiO and ZnS&NC/SiO before cycling. (b) The equivalent circuit model of electrodes.

https://doi.org/10.1021/acsomega.4c11551
ACS Omega 2025, 10, 17642−17650

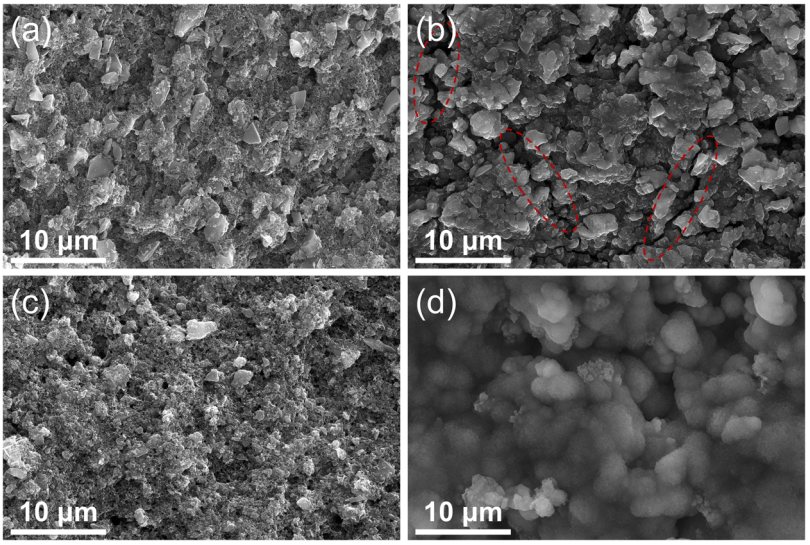

Figure 8. SEM images of SiO pole piece (a) before cycling and (b) after 1000 cycles, ZnS&NC/SiO pole piece (c) before cycling and (d) after 1000 cycles.

the reversible capacity of ZnS&NC/SiO was still 776 mAh·g^{-1} at the end of the 100th cycle, which was much higher than those of SiO (65.80 mAh·g^{-1}) and ZnS&NC (325.56 mAh·g^{-1}). The outstanding lithium storage performance of ZnS&NC/SiO electrodes should be attributed to the synergistic effect between SiO and ZnS, which greatly alleviates the stress effect during lithium intercalation and improves the electrochemical performance. Moreover, the nitrogen-doped carbon can alleviate the volume expansion during lithium intercalation, enhance the conductivity of electrode materials, and accelerate the transmission speed of lithium ions.

Figure 6b shows the rate capabilities of pristine SiO, ZnS&NC, and ZnS&NC/SiO at different current densities. Owing to the instability of SiO, its reversible capacity rapidly declined as the current density increased from 0.1 to 2.0 A·g^{-1} in subsequent cycles and only returned to a low level when the current density reduced back to 0.1 A·g^{-1}. In contrast, the reversible capacity of ZnS&NC and ZnS&NC/SiO samples exhibited less decay during the increase in current density and retained a high reversible capacity when the current density was reduced back to 0.1 A·g^{-1}. Particularly, The reversible specific capacity of the ZnS&NC/SiO sample was 944, 849, 692, 528, and 375 mAh·g^{-1} at current densities of 0.1, 0.2, 0.5, 1.0, and 2.0 A·g^{-1}, respectively. This demonstrates that ZnS&NC/SiO exhibits exceptional electrochemical reversibility and outstanding rate performance.

Figure 6c shows the cycling stability of the ZnS&NC/SiO at a current density of 1.0 A·g^{-1} over 1000 cycles. Prior to the main test, the electrode was subjected to four initial cycles at a current density of 0.1 A·g^{-1} for activation, followed by a long cycle test at the current density of 1.0 A·g^{-1}. The result indicates that the ZnS&NC/SiO sample maintains a high reversible capacity and exhibits excellent cycle stability, with the reversible capacity remaining at 748 mAh·g^{-1} after 1000 cycles. The enhanced reversible capacity can be attributed to the absence of significant cracks or voids on the surface of the ZnS&NC/SiO composite electrode. Based on the summary of reported electrochemical properties for SiO_x/metal compound electrodes used as anode materials in lithium-ion batteries (Table 1), it is obvious that the cycle performance of the ZnS&NC/SiO anode material developed in this study surpasses that of the majority of current SiO_x/metal compound anode materials.

Electrochemical impedance spectroscopy (EIS) measurements, a valuable means for identifying the kinetics of lithium intercalation/deintercalation into electrodes, were performed on the pristine SiO and ZnS&NC/SiO electrodes, as illustrated in Figure 7. Figure 7a shows Nyquist plots for SiO and ZnS&NC/SiO samples, along with the construction of an equivalent electrical circuit model to simulate the impedance behavior of electrodes within half-cell configurations (Figure 7b). The interception of the Z' axis at the high-frequency range is attributed to the ohmic resistance (Rs), corresponding to the electrolyte's inherent resistance. A semicircular line observed within the midfrequency range is attributed to the charge transfer resistance (Rct). The straight-sloping line in the lower frequency represents the Warburg impedance (Z_W), corresponding to the lithium-ion diffusion at the electrode/electrolyte interfaces.[48,49] Calculations reveal that the ZnS&NC/SiO sample (Rct = 62 Ω) exhibit a significantly lower charge transfer resistance compared to the SiO sample (Rct = 417 Ω), indicating the improved interfacial properties and electrode reaction kinetics by coating zinc sulfide and nitrogen-doped carbon.

To gain deeper insights into the outstanding cycle performance of ZnS&NC/SiO, the morphology of the electrodes before and after 1000 cycles was analyzed through SEM, as shown in Figure 8. Wide cracks and gaps appeared on the surface of the pristine SiO after 1000 cycles of charge−discharge, which can be primarily attributed to the continuous volume expansion and contraction of the active material in the battery, resulting in an incomplete electrode structure and insufficient interparticle contact. In contrast, no obvious crack or gap was found on the surface of the ZnS&NC/SiO electrode after 1000 cycles. These results illustrate that the unique structural design effectively inhibits electrode fragmentation and fracturing during charge−discharge cycles, thereby extending the electrode's cycle life.

Based on the above discussion, the mechanism for the benign lithium storage performance of the ZnS&NC/SiO composite was suggested. First, benefiting from the unique structural design, nitrogen-doped carbon and ZnS were coated

https://doi.org/10.1021/acsomega.4c11551
ACS Omega 2025, 10, 17642−17650

on the surface of SiO through the decomposition of Zn-MOF during heat treatment. Benefiting from the different lithium intercalation potentials between SiO and ZnS, one of them can serve as a buffer medium to alleviate volume expansion and inhibit agglomeration when the other material undergoes lithium intercalation, leading to improved structural stability and promoted electrochemical performance of the electrode. Moreover, introducing nitrogen-doped carbon can effectively improve the electrical conductivity of the material and increase more active sites, leading to increased participation of active materials in the electrochemical processes.

4. CONCLUSIONS

In summary, a composite material of SiO coated with zinc sulfide and nitrogen-doped carbon (ZnS&NC/SiO) was successfully prepared. The synthesis process involved the first in situ growth of Zn-MOF on the surface of SiO via a hydrothermal method, followed by high-temperature heat treatments. The ZnS&NC/SiO composite exhibits exceptional electrochemical properties for lithium-ion storage, including high reversible capacity, small charge transfer resistance, superior rate capability, and robust cyclability. The outstanding cycle stability is attributed to the synergistic effect between the introduced ZnS and nitrogen-doped carbon. This work provides a promising strategy for preparing anode materials with excellent cycling performance, which will accelerate the development of anode materials in Li-ion batteries.

AUTHOR INFORMATION

Corresponding Authors

Liu Feng − *Analysis and Testing Center, Shandong University of Technology, Zibo 255000 Shandong, China*; Email: willow-feng@163.com

Xuliang Zhang − *Analysis and Testing Center, Shandong University of Technology, Zibo 255000 Shandong, China*; Email: 1161485590@qq.com

Authors

Yongchao Liu − *School of Materials Science and Engineering, Shandong University of Technology, Zibo 255000 Shandong, China*; orcid.org/0009-0002-7269-7516

Hongliang Mu − *School of Materials Science and Engineering, Shandong University of Technology, Zibo 255000 Shandong, China; Shandong Kaisheng New Materials Co., Ltd, Zibo 255000 Shandong, China*

Wuhong Xin − *Analysis and Testing Center, Shandong University of Technology, Zibo 255000 Shandong, China*

Jinye Niu − *Analysis and Testing Center, Shandong University of Technology, Zibo 255000 Shandong, China*

Yong Wang − *Shandong Kaisheng New Materials Co., Ltd, Zibo 255000 Shandong, China*

Guanghui Li − *Shandong Kaisheng New Materials Co., Ltd, Zibo 255000 Shandong, China*

Complete contact information is available at: https://pubs.acs.org/10.1021/acsomega.4c11551

Notes

The authors declare no competing financial interest.

ACKNOWLEDGMENTS

This study was supported by the National Natural Science Funds (No. 22002074).

REFERENCES

(1) Kennedy, B.; Patterson, D.; Camilleri, S. Use of lithium-ion batteries in electric vehicles. *J. Power Sources* **2000**, *90* (2), 156−162.

(2) Ritchie, A. Recent developments and future prospects for lithium rechargeable batteries. *J. Power Sources* **2001**, *96* (1), 1−4.

(3) Wang, Y.; Liu, B.; Li, Q.; Cartmell, S.; Ferrara, S.; Deng, Z. D.; Xiao, J. Lithium and lithium ion batteries for applications in microelectronic devices: A review. *J. Power Sources* **2015**, *286*, 330−345.

(4) Chen, Y.; Kang, Y.; Zhao, Y.; Wang, L.; Liu, J.; Li, Y.; Liang, Z.; He, X.; Li, X.; Tavajohi, N.; Li, B. A review of lithium-ion battery safety concerns: The issues, strategies, and testing standards. *J. Energy Chem.* **2021**, *59*, 83−99.

(5) Ali, M. A.; Farid, A.; Rasheed, A.; Yousaf, M.; Alfares, A. M.; Ayub, N.; Khan, I.; Ghanem, M. A.; Marken, F. Synthesis and electrochemical properties of microcanals Mg-S-Cu-S as an electrode material for energy storage applications. *J. Electroanal. Chem.* **2024**, *971*, No. 118588.

(6) Yousaf, M.; Rasheed, A.; Farid, A.; Khan, I.; Ghanem, M. A.; Marken, F. Electrochemical properties of binder-free micro-blocks/sheets-based cadmium-nickel-sulfide electrode materials for portable energy storage applications. *J. Energy Storage* **2024**, *99*, No. 113416.

(7) Atta, S.; Rasheed, A.; Farid, A.; Yousaf, M.; Raza, A.; Khan, I.; Ghanem, M. A.; Marken, F. Electrochemical performance of cauliflower like binder-free magnesium-sulphide-electrodes for super-capacitor application. *J. Saudi Chem. Soc.* **2024**, *28* (5), No. 101904.

(8) He, Q.; Ashuri, M.; Liu, Y.; Liu, B.; Shaw, L. Silicon microreactor as a fast charge, long cycle life anode with high initial coulombic efficiency synthesized via a scalable method. *ACS Appl. Energy Mater.* **2021**, *4* (5), 4744−4757.

(9) Ashuri, M.; He, Q.; Shaw, L. L. Silicon oxides for Li-ion battery anode applications: toward long-term cycling stability. *J. Power Sources* **2023**, *559*, No. 232660.

(10) Fu, R.; Ji, J.; Yun, L.; Jiang, Y.; Zhang, J.; Zhou, X.; Liu, Z. Graphene wrapped silicon suboxides anodes with suppressed Li-uptake behavior enabled superior cycling stability. *Energy Storage Mater.* **2021**, *35*, 317−326.

(11) Shi, L.; Pang, C.; Chen, S.; Wang, M.; Wang, K.; Tan, Z.; Gao, P.; Ren, J.; Huang, Y.; Peng, H.; Liu, Z. Vertical graphene growth on SiO microparticles for stable lithium ion battery anodes. *Nano Lett.* **2017**, *17* (6), 3681−3687.

(12) Wang, L.; Tang, Q.; Zhao, C.; Zhang, S.; Zhao, H. Fabrication and application of network-liked carbon coated SiO as anode material for lithium ion batteries. *Mater. Lett.* **2023**, *345*, No. 134446.

(13) Zhang, Q.; Xi, B.; Xiong, S.; Qian, Y. Carbon coated SiO nanoparticles embedded in hierarchical porous N-doped carbon nanosheets for enhanced lithium storage. *Inorg. Chem. Front.* **2021**, *8*, 4282−4290, DOI: 10.1039/D1QI00778E.

(14) Nguyen, T. L.; Hur, J.; Kim, I. T. Facile Synthesis of quantum dots SnO_2/Fe_3O_4 hybrid composites for superior reversible lithium-ion storage. *J. Ind. Eng. Chem.* **2019**, *72*, 504−511.

(15) Kong, X.; Su, Y.; Xing, C.; Cheng, W.; Huang, J.; Zhang, L.; Ouyang, H.; Feng, Q. Facile synthesis of porous TiO_2/SnO_2 nanocomposite as lithium ion battery anode with enhanced cycling stability via nanoconfinement effect. *Chin. Chem. Lett.* **2024**, *35* (11), No. 109428.

(16) Chen, L.; Tang, B.; Li, H.; Wang, B.; Huang, B. Porous SnO_2/Co_3O_4 nanocubes anchored onto reduced graphene oxide as a high-performance anode for lithium-ion batteries. *Solid State Ionics* **2023**, *396*, No. 116241.

(17) Ma, Y. Sol-gel synthesis of ZnO/TiO_2 core-shell nano-composites and their structural and electrochemical characterization as anode for lithium ion battery. *Int. J. Electrochem. Sci.* **2020**, *15* (12), 12559−12568.

(18) Gu, C.; Hong, Y.; Wang, X.; Joo, S. W.; Ren, H.; Huang, J. Fabrication of hollow SnO_2/ZnS@ C nanocubes as anode materials for advanced lithium-ion battery. *J. Alloys Compd.* **2021**, *878*, No. 160375.

(19) Bo, D.; Xuanning, H.; Zhenfei, C.; Yangzhou, M.; Guangsheng, S.; Weidong, Y.; Cuie, W. Effects of binders on electrochemical properties of high capacity silicon composite anodes. *Inorg. Chem. Commun.* **2020**, *113*, No. 107771.
(20) Kim, J.-H.; Sohn, H.-J.; Kim, H.; Jeong, G.; Choi, W. Enhanced cycle performance of SiO-C composite anode for lithium-ion batteries. *J. Power Sources* **2007**, *170* (2), 456−459.
(21) Woo, J.; Baek, S.-H.; Park, J.-S.; Jeong, Y.-M.; Kim, J. H. Improved electrochemical performance of boron-doped SiO negative electrode materials in lithium-ion batteries. *J. Power Sources* **2015**, *299*, 25−31.
(22) Liu, B. D.; Yang, B.; Dierre, B.; Sekiguchi, T.; Jiang, X. Local defect-induced red-shift of cathodoluminescence in individual ZnS nanobelts. *Nanoscale* **2014**, *6* (21), 12414−12420.
(23) Trung, D.; Tran, M.; Tu, N.; Thu, L.; Huyen, N.; Hung, N.; Viet, D.; Kien, N.; Huy, P. Synthesis, structural and optical properties of ZnS/ZnO heterostructure-alloy hexagonal micropyramids. *Opt. Mater.* **2022**, *125*, No. 112077.
(24) Wei, C.; Fei, H.; Tian, Y.; An, Y.; Tao, Y.; Li, Y.; Feng, J. Scalable construction of SiO/wrinkled MXene composite by a simple electrostatic self-assembly strategy as anode for high-energy lithium-ion batteries. *Chin. Chem. Lett.* **2020**, *31* (4), 980−983.
(25) Yang, Z.; Du, Y.; Yang, Y.; Jin, H.; Shi, H.; Bai, L.; Ouyang, Y.; Ding, F.; Hou, G.; Yuan, F. Large-scale production of highly stable silicon monoxide nanowires by radio-frequency thermal plasma as anodes for high-performance Li-ion batteries. *J. Power Sources* **2021**, *497*, No. 229906.
(26) Song, J.; Guo, S.; Kou, L.; Kajiyoshi, K.; Su, J.; Huang, W.; Li, Y.; Zheng, P. Controllable synthesis Honeycomb-like structure SiO_x/C composites as anode for high-performance lithium-ion batteries. *Vacuum* **2021**, *186*, No. 110044.
(27) Hu, X.; Liu, Y.; Chen, J.; Yi, L.; Zhan, H.; Wen, Z. Fast redox kinetics in bi-heteroatom doped 3D porous carbon nanosheets for high-performance hybrid potassium-ion battery capacitors. *Adv. Energy Mater.* **2019**, *9* (42), No. 1901533.
(28) Yu, B.; Ji, Y.; Hu, X.; Liu, Y.; Yuan, J.; Lei, S.; Zhong, G.; Weng, Z.; Zhan, H.; Wen, Z. Heterostructured Cu_2S@ ZnS/C composite with fast interfacial reaction kinetics for high-performance 3D-printed Sodium-Ion batteries. *Chem. Eng. J.* **2022**, *430*, No. 132993.
(29) Janani, B.; Okla, M. K.; Abdel-Maksoud, M. A.; AbdElgawad, H.; Thomas, A. M.; Raju, L. L.; Al-Qahtani, W. H.; Khan, S. S. CuO loaded ZnS nanoflower entrapped on PVA-chitosan matrix for boosted visible light photocatalysis for tetracycline degradation and anti-bacterial application. *J. Environ. Manage.* **2022**, *306*, No. 114396.
(30) Li, F.; Li, W.; Li, J.; Xue, W.; Wang, Y.; Zhao, X. Investigation of supported Zn $(OAc)_2$ catalyst and its stability in N-phenyl carbamate synthesis. *Appl. Catal., A* **2014**, *475*, 355−362.
(31) Wiame, F.; Jasnot, F.-R.; Światowska, J.; Seyeux, A.; Bertran, F.; Le Fèvre, P.; Taleb-Ibrahimi, A.; Maurice, V.; Marcus, P. Oxidation of α-brass: A photoelectron spectroscopy study. *Surf. Sci.* **2015**, *641*, 51−59.
(32) Wang, D.; Gao, M.; Pan, H.; Wang, J.; Liu, Y. High performance amorphous-Si@ SiO_x/C composite anode materials for Li-ion batteries derived from ball-milling and in situ carbonization. *J. Power Sources* **2014**, *256*, 190−199.
(33) Yang, M.; Jin, L.; He, M.; Yi, Z.; Duan, T.; Yao, W. SiOx@C composites obtained by facile synthesis as anodes for lithium-and potassium-ion batteries with excellent electrochemical performance. *Appl. Surf. Sci.* **2021**, *542*, No. 148712.
(34) Liu, X.; Xu, Z.; Iqbal, A.; Chen, M.; Ali, N.; Low, C.; Qi, R.; Zai, J.; Qian, X. Chemical coupled PEDOT: PSS/Si electrode: suppressed electrolyte consumption enables long-term stability. *Nano-Micro Lett.* **2021**, *13*, 1−12.
(35) Kong, F.; He, X.; Liu, Q.; Qi, X.; Sun, D.; Zheng, Y.; Wang, R.; Bai, Y. Enhanced reversible Li-ion storage in Si@ Ti_3C_2 MXene nanocomposite. *Electrochem. Commun.* **2018**, *97*, 16−21.
(36) Zhang, L.; Zhang, Y.; Han, Y.; Yang, L.; Zou, G.; Zhao, H.; Hou, H.; Gu, G. Bead-milling and recrystallization from natural marmatite to Fe-doping ZnS-C materials for lithium-ion battery anodes. *Electrochim. Acta* **2021**, *399*, No. 139430.
(37) He, L.; Liao, X.-Z.; Yang, K.; He, Y.-S.; Wen, W.; Ma, Z.-F. Electrochemical characteristics and intercalation mechanism of ZnS/C composite as anode active material for lithium-ion batteries. *Electrochim. Acta* **2011**, *56* (3), 1213−1218.
(38) Ma, Y.; Ma, Y.; Geiger, D.; Kaiser, U.; Zhang, H.; Kim, G.-T.; Diemant, T.; Behm, R. J.; Varzi, A.; Passerini, S. ZnO/$ZnFe_2O_4$/N-doped C micro-polyhedrons with hierarchical hollow structure as high-performance anodes for lithium-ion batteries. *Nano Energy* **2017**, *42*, 341−352.
(39) Tian, G.; Zhao, Z.; Sarapulova, A.; Das, C.; Zhu, L.; Liu, S.; Missiul, A.; Welter, E.; Maibach, J.; Dsoke, S. Understanding the Li-ion storage mechanism in a carbon composited zinc sulfide electrode. *J. Mater. Chem. A* **2019**, *7* (26), 15640−15653.
(40) Zhou, N.; Wu, Y.; Zhou, Q.; Li, Y.; Liu, S.; Zhang, H.; Zhou, Z.; Xia, M. Enhanced cycling performance and rate capacity of SiO anode material by compositing with monoclinic TiO_2 (B). *Appl. Surf. Sci.* **2019**, *486*, 292−302.
(41) Xia, M.; Yi-ran, L.; Xiong, X.; Hu, W.; Tang, Y.-w.; Zhou, N.; Zhou, Z.; Zhang, H.-b. Enhancing the electrochemical performance of micron-scale SiO@C/CNTs anode via adding piezoelectric material BaTiO3 for high-power lithium ion battery. *J. Alloys Compd.* **2019**, *800*, 116−124.
(42) Zhang, Y.; Guo, G.; Chen, C.; Jiao, Y.; Li, T.; Chen, X.; Yang, Y.; Yang, D.; Dong, A. An affordable manufacturing method to boost the initial Coulombic efficiency of disproportionated SiO lithium-ion battery anodes. *J. Power Sources* **2019**, *426*, 116−123.
(43) Wang, T.; Chen, Z.; Chen, D.; Zhao, R. Hybrid MnO-SiO_x@ C microspheres with a hierarchical mesoporous structure for advanced lithium-ion battery anodes. *J. Alloys Compd.* **2022**, *899*, No. 163251.
(44) He, Z.; Huang, J.; Liu, K.; Tang, X.; Dai, Y. Fabrication of nanofibrous SiO_x/C/CoO composites with fast reaction kinetic and excellent structural stability for lithium storage. *J. Alloys Compd.* **2019**, *811*, No. 151971.
(45) Dou, F.; Shi, L.; Song, P.; Chen, G.; An, J.; Liu, H.; Zhang, D. Design of orderly carbon coatings for SiO anodes promoted by TiO_2 toward high performance lithium-ion battery. *Chem. Eng. J.* **2018**, *338*, 488−495.
(46) Cheng, F.; Wang, G.; Sun, Z.; Yu, Y.; Huang, F.; Gong, C.; Liu, H.; Zheng, G.; Qin, C.; Wen, S. Carbon-coated SiO/ZrO_2 composites as anode materials for lithium-ion batteries. *Ceram. Int.* **2017**, *43* (5), 4309−4313.
(47) Zhang, H.; Hu, R.; Liu, Y.; Cheng, X.; Liu, J.; Lu, Z.; Zeng, M.; Yang, L.; Liu, J.; Zhu, M. Highly reversible conversion reaction in Sn_2Fe@SiO_x nanocomposite: A high initial Coulombic efficiency and long lifetime anode for lithium storage. *Energy Storage Mater.* **2018**, *13*, 257−266.
(48) Jiang, Q.; Liu, D.; Zhang, H.; Wang, S. Plasma-assisted sulfur doping of $LiMn_2O_4$ for high-performance lithium-ion batteries. *J. Phys. Chem. C* **2015**, *119* (52), 28776−28782.
(49) Jiang, Q.; Zhang, H.; Wang, S. Plasma-enhanced low-temperature solid-state synthesis of spinel $LiMn_2O_4$ with superior performance for lithium-ion batteries. *Green Chem.* **2016**, *18* (3), 662−666.

https://doi.org/10.1021/acsomega.4c11551
ACS Omega 2025, 10, 17642−17650